

On the low frequency flexural band gaps of a metamaterial plate with low porosity

Chaitanya Morey,^{1, a)} Sundararajan Natarajan,^{1, b)} and Chandramouli Padmanabhan^{1, c)}

*Department of Mechanical Engineering, Indian Institute of Technology Madras,
Chennai-600036.*

(Dated: 17 December 2024)

This paper demonstrates numerically and experimentally that it is possible to tailor flexural band gaps in the low-frequency regime by appropriate choice of cutout characteristics. The finite element method is used to obtain the numerical dispersion relation and band gaps. The influence of the cutout's shape, size, and location on the band gap is systematically studied. The study demonstrates that the cutout should pass through the center of the unit cell, and a large aspect ratio is required to introduce flexural band gaps in the low-frequency regime. This is validated by experiments on a finite plate with 3×3 unit cells.

^{a)}Electronic mail: me20d017@smail.iitm.ac.in

^{b)}Electronic mail: snatarajan@iitm.ac.in.

^{c)}Electronic mail: mouli@iitm.ac.in

I. INTRODUCTION

Metamaterials are engineered periodic structures with tailored features that has properties not commonly found in conventional materials, such as negative mass density, negative Poisson's ratio, high specific stiffness and negative thermal expansions.^{1,6,21} The properties of the metamaterials are derived from the geometric design, which could be tailored according to the needs. By intelligently engineering the macro- and/or the micro-structure, the metamaterials can be used in vibration isolation³⁰, noise filtering¹⁷, wave guiding¹², seismic isolation¹⁰, to name a few. This is due to the presence of 'band gaps', which attenuates the wave passing through the structure. The band gaps could be of either electromagnetic waves, elastic waves or acoustic waves. Thanks to the advancements in additive manufacturing, realization of band gaps is now possible.

Xiao et al,²⁶ studied the flexural vibration in thin plates with two-dimensional ternary locally resonant structures. Xiong et al.,²⁸ designed periodic elastic metamaterial by the locally resonant band-gap mechanism. An asymptotic optimization method was employed to achieve required band gaps. Li et al.,¹⁴ demonstrated that the presence of low-frequency band gap in thick elastic steel plate. This was achieved by adopting double-sided composite stepped resonators, which contain an array of rubber fillers embedded in a thick steel plate. Zhang et al.,³² proposed a tunable pneumatic metamaterial plate with airbag local resonators to widen the band gap below 100 Hz. Xue et al.,²⁹ proposed a plate-type local resonator integrated with a base plate for vibration location and suppression. Yin et al.,³¹ designed a new three-dimensional elastic metamaterial with surface resonant units using 3D printing technology. Chen et al.,² employed a sandwich construction for isolating low-frequency vibration and flexural wave propagation in ship structures. Dal Paggetto and Serpa¹⁸ studied band gaps in a ternary periodic metamaterial using a plane wave expansion method. The plate kinematics was based on Mindlin plate theory, and the unit cell had the following materials: acrylonitrile-butadiene-styrene (ABS), low-density polyethylene, and lead. Li et al.,¹³ proposed a multi-band gap metamaterial for vibration suppression by integrating membrane-mass structures into a honeycomb sandwich structure.

In recent years, the investigation of porous metamaterials has increased due to its lightweight and ease of manufacturing. The effects of porous fractal phononic crystals and hierarchy on

band gaps have also been studied. Wang et al.²⁴ examined the impact of fractal hierarchy on the in-plane wave band structure of Sierpinski triangular fractal porous phononic crystal (FPPC). Two types of Sierpinski triangle fractals were considered in their study: an equilateral triangle and a right-angled isosceles triangle. For the same level of fractal hierarchy, the Sierpinski equilateral triangle FPPC has wider band gaps. At the same time, at lower porosity (15%), the first band opens, and also, a relatively lower band gap can be obtained with Sierpinski right-angle isosceles FPPC with a porosity of 70%. The lowest band achieved is around 27 kHz for a unit cell with a dimension of 20 mm; the material used is aluminum. But this is achieved only at a high porosity of 60% or more. Liu et al.¹⁶ investigated the influence of T-square fractal holes on the in-plane band structure. The T-square fractal unit cell at the second level of the hierarchy has the same geometry used by Li et al.¹⁵. At the fourth level, where the porosity is almost 80%, the lowest band gap achieved is around the 5th/6th mode. For lower porosities, the band gaps appear at higher modes. The unit cell is 10 mm in dimension and aluminum is used for in-plane studies. Shi et al.¹⁹ studied the structural hierarchy of in-plane and out-of-plane band structures with tetrad elliptical patterns in perforated plates. They obtained band gaps for three levels of perforations; level 2 showed the maximum number of band gaps for a 52.3% porosity. It must be noted that the lowest band gap occurs between the 10/11th modes and the numerical results were validated experimentally.

Jin et al.¹¹ studied the flexural band gap properties of corrugated plates sandwiched between two plates with spiral holes. While they demonstrated low-frequency band gaps, the structure developed is quite complex, with a combination of aluminum and resin material in the spiral pockets. Das et al.⁴ investigated the flexural band gaps of plates with different periodic cavity shapes (circular, square, vertical rectangle and horizontal rectangle). The simulation results were validated with experiments. It was observed that changing the aspect ratio significantly affects bands; by decreasing the aspect ratio, the width of the band gap can be increased. Around 750 Hz, the lowest band was obtained with a horizontal rectangle-shaped cavity. Javid et al.⁹ are possibly among the earliest researchers to look at the effects of low porosity levels on band gaps of periodic structures. They examined alternating orthogonal elliptical holes with 1%, 5%, and 10% porosity levels. High aspect ratios enable them to demonstrate band gaps beyond the 6th mode for 5% porosity. Tian et al.²³ studied the orientation effect on the band gaps of the low-porosity perforated plates. The numerical results were verified with experiments, and the

lowest in-plane band gap obtained is in the 3.4–4.1 kHz frequency range for 4.8% porosity. Chen et al.³ proposed a new auxetic perforated metamaterial with low porosity that shows negative Poisson’s ratio and band gap properties. The results show that the proposed configuration has enhanced tensile strength, and the chord length of the perforation has a significant impact on widening the band gap characteristics.

From the discussions above, it is clear that one can generate wider band gaps either by higher porosity structures or by using binary or ternary material configurations. Moreover, the band gaps were reported beyond the 7th or 8th mode of a unit cell, primarily focusing on in-plane wave propagation. Only a few papers have been published focusing on periodic structures with low porosity. Again, in these papers, it is found that band gaps start appearing only after the 6th or the 7th mode. The challenge remains as to how to get these band gaps to lower modes, for example, in the 2nd or 3rd mode while keeping low porosity ($< 10\%$). Further, to achieve elastic wave attenuation, different types of metamaterials have been studied; with local resonator^{27,33}, embedded with scatterer^{8,30}, or acoustic black holes^{5,22}.

In this study, we are interested in elastic band gaps formed by elastic waves passing through the solid due to dynamic excitations. The primary objective of the research reported in this paper is to generate the flexural band gaps in low-frequency regions (encompassing the first ten modes of the structure and typically in the 30-300 Hz range) without employing resonators or scatterers or secondary material. A detailed parametric investigation of various shapes shows that a cross shape with a high aspect ratio can generate low-frequency band gaps with low porosity of the unit cell metamaterial. The numerical predictions are validated with experiments on a finite plate with 3×3 unit cells.

The rest of the paper is organized as follows: the plate kinematics, the Bloch periodic boundary condition, and the finite element discretization are discussed in Section II. Section III presents the flexural band gaps obtained from the numerical study. The experimental setup and the comparison between the experiments and the numerical simulation is presented in Section IV, followed by significant conclusions from this study in the last section.

II. THEORETICAL FORMULATION

An isotropic homogeneous plate does not exhibit band gap characteristics, while a plate with a cutout introduces band gap²⁵. Consider a plate with a cutout to understand the flexural band gap characteristics. The plate kinematics is based on the Reissner-Mindlin plate theory (RMPT), an extension of the Kirchhoff-Love plate theory. The RMPT is preferred over the latter, as it accommodates the use of C^0 shape functions within the framework of the finite element method. This section presents a brief overview of the RMPT, followed by a description of spatial discretization and enforcement of Bloch periodicity.

A. Basics of Reissner-Mindlin plate theory

Consider a mid-plane of an isotropic homogeneous elastic plate of uniform thickness, h , occupying the domain $\Omega \subset \mathbb{R}^2$, bounded by one-dimensional surface, $\partial\Omega$, see Figure 1. Let the

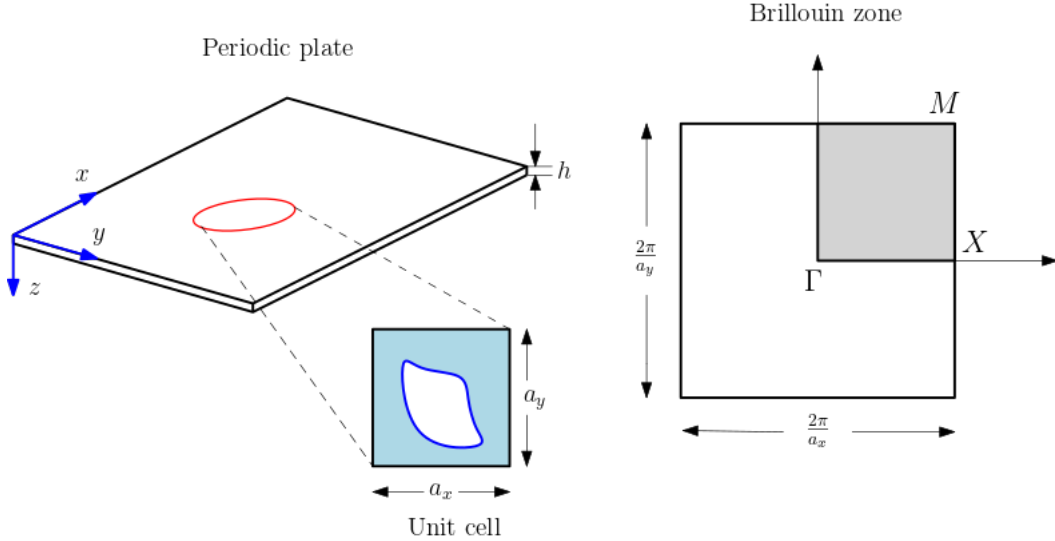


FIG. 1: Schematic of a periodic plate with uniform thickness, h with its unit cell with an arbitrary cutout and the first irreducible Brillouin zone

coordinates of a point be denoted by $\mathbf{x} = (x, y, z)$ and let the transverse displacement and the rotations normal to the midplane be denoted by $w(\mathbf{x})$ and $\boldsymbol{\beta}(\mathbf{x}) = (\beta_x, \beta_y)$, respectively. The

midplane displacements and the independent rotations within the RMPT are given by:

$$\begin{aligned} u(\mathbf{x}, t) &= z\beta_x(x, y, t) \\ v(\mathbf{x}, t) &= z\beta_y(x, y, t) \\ w(\mathbf{x}, t) &= w(x, y, t) \end{aligned} \quad (1)$$

The bending strain ($\boldsymbol{\varepsilon}_b$) and the shear strain ($\boldsymbol{\varepsilon}_s$) are given by:

$$\boldsymbol{\varepsilon}_b = \begin{Bmatrix} \frac{\partial\beta_x}{\partial x} \\ \frac{\partial\beta_y}{\partial y} \\ \frac{\partial\beta_x}{\partial y} + \frac{\partial\beta_y}{\partial x} \end{Bmatrix}; \quad \boldsymbol{\varepsilon}_s = \begin{Bmatrix} \gamma_{xz} \\ \gamma_{yz} \end{Bmatrix} = \begin{Bmatrix} \beta_x + \frac{\partial w}{\partial x} \\ \beta_y + \frac{\partial w}{\partial y} \end{Bmatrix} \quad (2)$$

The bending and shear strains are related to the moment resultants, $\mathbf{M} = \{M_x, M_y, M_{xy}\}$ and the shear forces $\mathbf{T} = \{T_x, T_y\}$, respectively, are related through:

$$\mathbf{M} = \underbrace{\frac{Eh^3}{12(1-\nu^2)} \begin{bmatrix} 1 & \nu & 0 \\ \nu & 1 & 0 \\ 0 & 0 & \frac{1-\nu}{2} \end{bmatrix}}_{\mathbf{H}_b} \boldsymbol{\varepsilon}_b \quad \text{and} \quad \mathbf{T} = \underbrace{\kappa Gh \begin{bmatrix} 1 & 0 \\ 0 & 1 \end{bmatrix}}_{\mathbf{H}_s} \boldsymbol{\varepsilon}_s \quad (3)$$

where κ is the shear correction factor, $G = E/(2(1 + \nu))$ the bulk modulus, E is the Young's modulus and Poisson's ratio is represented by ν . In this paper, we adopt the Hellinger-Reissner function to develop the n -noded plate element and the total strain energy function, $\Pi(\mathbf{u})$, is given by:

$$\Pi(\mathbf{u}) = \frac{1}{2} \int_{\Omega} \{ \boldsymbol{\varepsilon}_b^T \mathbf{H}_b \boldsymbol{\varepsilon}_b + \boldsymbol{\varepsilon}_s^T \mathbf{H}_s \boldsymbol{\varepsilon}_s \} d\Omega - \int q w d\Omega + \Pi_{\text{ext}} \quad (4)$$

where $\mathbf{u} = \{w, \beta_x, \beta_y\}$ is the vector of the degrees-of-freedom (Dofs) associated with the displacement field in a finite element discretization; the influence of external forces and boundary is contained in Π_{ext} and q is the transverse loading. The kinetic energy of the plate is given by:

$$T(\mathbf{u}) = \frac{1}{2} \int_{\Omega} \left\{ p(\dot{w}^2 + \dot{v}^2 + \dot{w}^2) + I(\dot{\beta}_x^2 + \dot{\beta}_y^2) \right\} d\Omega \quad (5)$$

where $(\dot{\cdot})$, represents the time derivative of the variable, $p = \int_{-h/2}^{h/2} \rho(z) dz$, $I = \int_{-h/2}^{h/2} z^2 \rho(z) dz$ and $\rho(z)$ is the mass density that varies through the thickness of the plate. In this work, the domain is partitioned into non-overlapping elements Ω^h , and on using shape functions that

span at least the linear space, the transverse displacement, w and the independent rotations, β_x, β_y are written as:

$$(w, \beta_x, \beta_y) = \sum_{i=1}^n \lambda_i (w_i, \beta_{x_i}, \beta_{y_i}) \quad (6)$$

where λ_i are the shape functions. For spatial discretization, the domain is discretized with 4-noded bilinear quadrilateral element with 3 dofs, viz., (w, β_x, β_y) per node. To alleviate the shear locking phenomenon, a field consistent shear flexible element is used²⁰. Upon substituting Equation (6) in Equations (4) and (5) and assuming harmonic solution $\mathbf{u} = \mathbf{u}_o e^{-i\omega t}$ for the unknown field is assumed and following standard Galerkin procedure, we get the following eigenvalue problem:

$$(\mathbf{K} - \omega^2 \mathbf{M}) \mathbf{u}_o = \mathbf{0} \quad (7)$$

where $\mathbf{K} = \mathbf{K}_b + \mathbf{K}_s$ is the stiffness matrix that is an additive combination of the stiffness corresponding to the bending and shear, \mathbf{M} is the mass matrix and ω is the frequency.

B. Bloch Periodic boundary condition

In this study, our focus is to generate flexural band gaps in the low frequency regime, wherein the domain kinematics is based on RMPT. Since this is a two-dimensional structure, and assuming the periodicity to be in the x - and y -directions, the elastic waves propagate in the xy plate, it should satisfy:

$$\mathbf{u}(\mathbf{r}) = e^{i\mathbf{k}\cdot\mathbf{r}} \mathbf{u}_{\mathbf{k}}(\mathbf{r}) \quad (8)$$

where \mathbf{k} is the first irreducible Brillouin zone, $\mathbf{u}_{\mathbf{k}}(\mathbf{r})$ is the vector function containing the degree-of-freedom and \mathbf{r} is the position vector.

Figure 2 shows a representative unit cell. The nodes on the boundary are grouped into eight categories, viz., $\mathbf{u}_{\ell b}$, \mathbf{u}_b , \mathbf{u}_{rb} , \mathbf{u}_r , \mathbf{u}_{rt} , \mathbf{u}_t , $\mathbf{u}_{\ell t}$ and \mathbf{u}_{ℓ} , where the subscripts ℓ , r , b , t represents the displacements corresponding to the left, right, bottom and top nodes of the unit cell. Note that the corner nodes are represented with a double subscript. All the interior nodes are grouped in \mathbf{u}_{in} . Using Equation (8), the displacement relations between the about categories is given by:

$$\begin{aligned} \mathbf{u}_r &= e^{ik_x a} \mathbf{u}_{\ell}, & \mathbf{u}_t &= e^{ik_y a} \mathbf{u}_b \\ \mathbf{u}_{rb} &= e^{ik_x a} \mathbf{u}_{\ell b}, & \mathbf{u}_{rt} &= e^{i(k_x + k_y)a} \mathbf{u}_{\ell b} \\ \mathbf{u}_{\ell t} &= e^{ik_y a} \mathbf{u}_{\ell b}. \end{aligned} \quad (9)$$

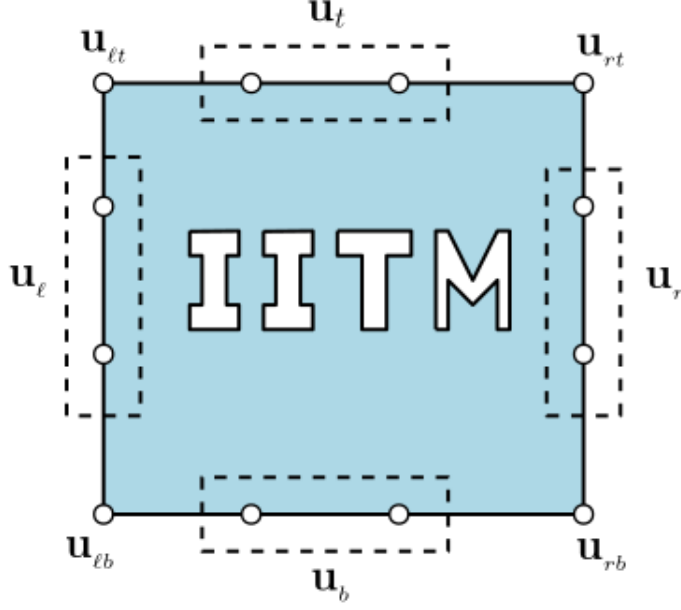


FIG. 2: Schematic representation of unit periodic cell and the notation for boundary nodes

According to the Bloch periodicity, the displacements in the domain can be related to the above eight categories through the following transformation matrix:

$$\mathbf{u}_o = \mathbf{T}\hat{\mathbf{u}} \quad (10)$$

where $\hat{\mathbf{u}} = \{\mathbf{u}_\ell, \mathbf{u}_b, \mathbf{u}_{\ell b}, \mathbf{u}_{rt}\}^T$ and the transformation matrix \mathbf{T} is given by:

$$\mathbf{T} = \begin{bmatrix} \mathbf{I} & \mathbf{0} & \mathbf{0} & \mathbf{0} \\ \mathbf{I}e^{k_x a} & \mathbf{0} & \mathbf{0} & \mathbf{0} \\ \mathbf{0} & \mathbf{I} & \mathbf{0} & \mathbf{0} \\ \mathbf{0} & \mathbf{I}e^{k_y a} & \mathbf{0} & \mathbf{0} \\ \mathbf{0} & \mathbf{I} & \mathbf{I} & \mathbf{0} \\ \mathbf{0} & \mathbf{I} & \mathbf{I}e^{k_x a} & \mathbf{0} \\ \mathbf{0} & \mathbf{I} & \mathbf{I}e^{k_y a} & \mathbf{0} \\ \mathbf{0} & \mathbf{I} & \mathbf{I}e^{(k_x+k_y)a} & \mathbf{0} \\ \mathbf{0} & \mathbf{I} & \mathbf{0} & \mathbf{I} \end{bmatrix} \quad (11)$$

Upon substituting Equation (10) into Equation (7), results in:

$$\mathbf{A}(k_x, k_y, \omega)\hat{\mathbf{u}} = \mathbf{0} \quad (12)$$

where $\mathbf{A}(k_x, k_y, \omega) = \left(\mathbf{T}^\dagger (\mathbf{K} - \omega^2 \mathbf{M}) \mathbf{T} \right)$ and ‘ \dagger ’ denotes the Hermitian transpose. By solving Equation (12), the eigen frequencies corresponding to a specific Bloch wave vector (k_x, k_y) can be computed. This is repeated for all Bloch wave vectors along the path $M - \Gamma - X - M$ (c.f. Figure 1), a band diagram can be constructed to determine the dispersion spectra of the considered unit cell.

III. NUMERICAL RESULTS AND DISCUSSION

A. Validation

To validate the accuracy of the present method, the results were compared with those from Huang et al.⁷. For this purpose, we consider a plate of size $a = 10$ cm, $h = 1$ cm with a cutout radius, $r = 4.5$ cm. The material is assumed to be homogeneous and isotropic with the following properties: density, $\rho = 1144.4$ kg/m³, Youngs’ modulus, $E = 3.228$ GPa and Poisson’s ratio, $\nu = 0.37$. The computational domain is discretized with 4-noded bilinear quadrilateral elements, care has been taken to have the same number of nodes on the boundary that facilitates the application of Bloch periodic boundary conditions. Based on a systematic study, a mesh consisting of 7227 degrees of freedom was found to be adequate to compute the dispersion curves. Figure 3 shows the dispersion curves for a square plate with a circular cutout, and the results from the present work are compared against the work of Huang et al.,⁷. Note that the authors have not mentioned the mesh size for their results. The simulation was also run on a relatively coarser mesh with 2664 degrees of freedom, and it is seen that the results from the present work are in close agreement with that of Huang et al.,⁷.

B. Effect of shape, size and location of cutouts

Many studies have focused on the porous metamaterial with a circular hole^{7,25}. However, to the best of the authors’ knowledge, the influence of the cutout’s shape, size, and location on the width and the number of band gaps have not been studied systematically. As mentioned earlier, this study focuses on band gaps in the lower frequency zones (within the first 3 to 4 modes). Hence, this study investigated a series of shapes, starting with an ellipse and progressively

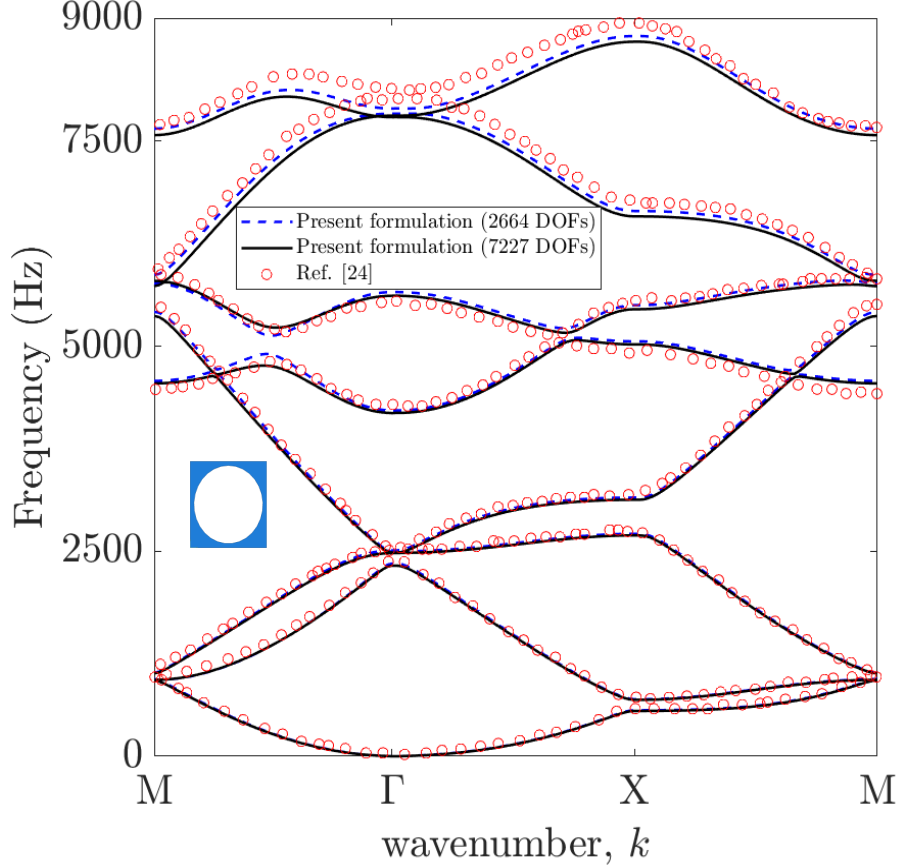


FIG. 3: Comparison of band gaps obtained from the present work with that of Huang et al.⁷.

moving to slender shapes with higher aspect ratios to understand their effect on the generation of band gaps in the low-frequency regime.

For the numerical study, the material used is Aluminum with Young's modulus, $E = 70$ GPa, density, $\rho = 2700$ kg/m³, and Poisson's ratio, $\nu = 0.33$. We consider a square unit cell with side length, $a = 330$ mm, and thickness, $h = 2$ mm. Six different configurations are considered to study the influence of cutout shape, size and location. Figure 4 shows the unit cells with different cutout shapes and the dimensions of the cutouts are given in Table I. Note that the dimensions for the cutouts, c.f. Figures 4b and 4f are arrived such that the area removed is the same, i.e., about 11% area is removed.

Figure 5 shows the dispersion curves for the considered cutout configurations. It seen from Figure 5a that for an elliptical cutout, no band gaps are present. Following this, the single ellipse is replaced by two high aspect ratio slender elliptical slots with their semi-major axes at

TABLE I: Unit cell with different configurations

Cavity shape	dimensions (in mm)
Ellipse	$b = 200, c = 100$
Intersection ellipses	$b = 200, c = 10$
Intersection rectangular slots	$b = 400, c = 15$
Cross	$b = 300, c = 20$
Unequal intersecting slots with centre offset	$b1 = 340, c1 = 17.72$ $b2 = 400, c2 = 15$
Intersecting rectangular slots with centre offset	$b = 340, c = 17.8$

90 degrees (c.f. Figure 4b). From Figure 5b, it can be seen that three band gaps are present between the 5th – 6th, 7th – 8th and 8th – 9th modes. In the case of intersecting rectangular slots, in addition to the band gaps that is present for the intersecting ellipses, band gaps also appear between the following modes: 1st – 2nd, 3rd – 4th, 4th – 5th. The maximum bandwidth of 37.86 Hz is observed between 5th – 6th, followed by the bandwidth of 19.02 Hz and 23.20 Hz between the 3rd – 4th and 4th – 5th, respectively.

It appears that removing material towards the corners and at the plate’s center affects the band gaps’ presence and size. Two more geometries are generated as in Figures 4e and 4f to understand this. In the first case, one of the rectangular slots is moved away from the center. So the area removed around the center has now been reduced. From Figure 5e multiple wide band gaps can be seen, but the band gaps below 100 Hz became narrower and band above 150 Hz becomes wider. In the following study, both the rectangular holes are moved away from the center while keeping the porosity the same. Figure 5f shows the dispersion curves for both the slots being offset from the center; it can be seen that the bands became narrower, and there are two narrow bands below 100 Hz. This would suggest that more material needs to be removed around the center area to generate wider band gaps in the lower frequencies (50–150 Hz).

The results imply that band gap generation is *highly* sensitive to the geometric shape and size of the cutouts. With low porosity and high aspect ratio, rectangular slots (along the diagonal and passing through the center of the plate) can generate multiple band gaps in the lower modes (first four). The porosity obtained with these diagonal slots is about 11%, rendering it

a practical solution for vibration isolation applications targeting low frequencies.

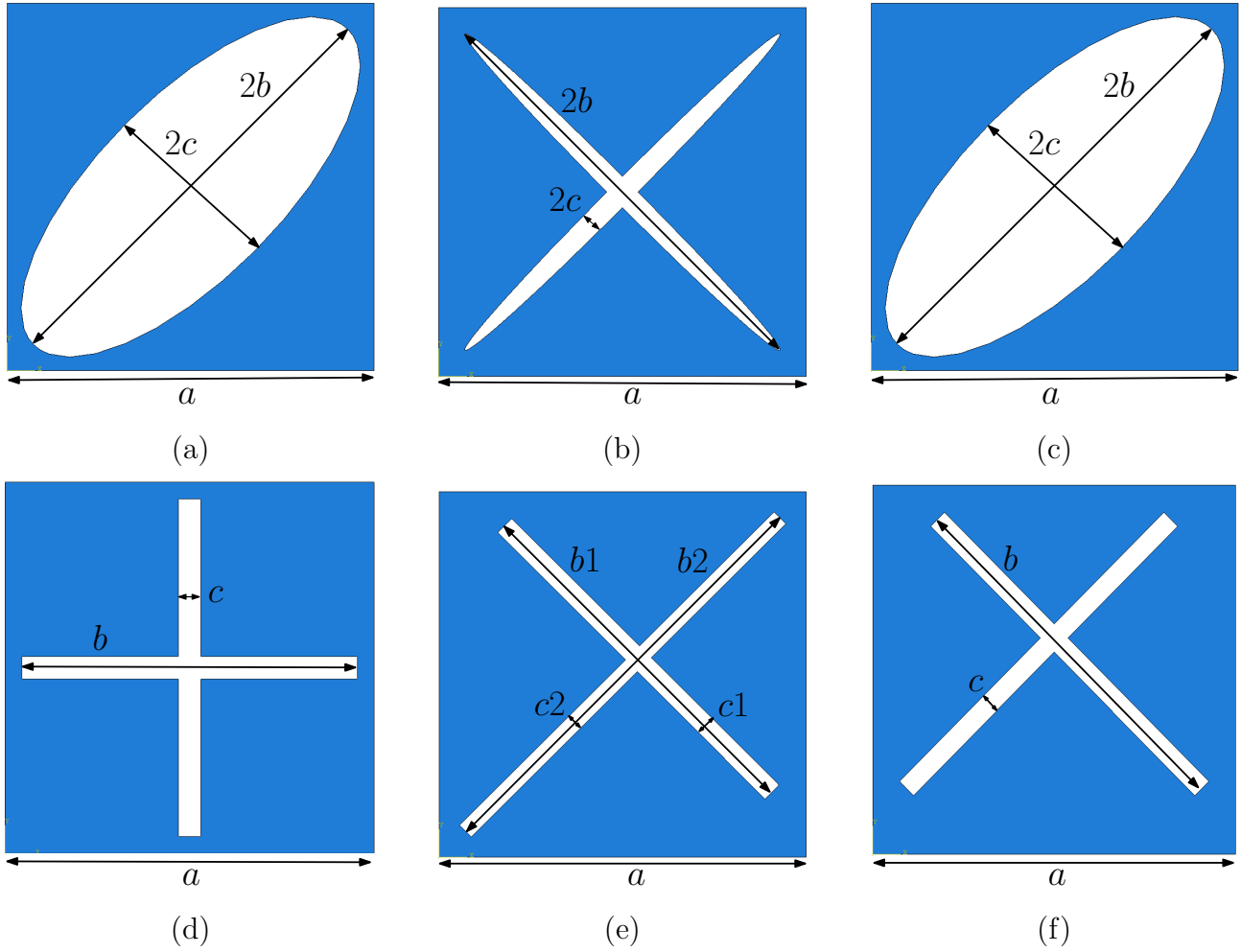


FIG. 4: Schematic representation of a unit cell with different cutout shapes: (a) ellipse, (b) intersecting ellipses, (c) intersecting rectangular slots, (d) cross, (e) unequal intersecting slots with centre offset and (f) Intersecting slots with centre offset.

IV. EXPERIMENTAL VERIFICATION

A. Experimental setup

To verify the numerical results, an experiment is carried out to examine the attenuation capabilities of the proposed low-porosity perforated plate. An aluminum square plate with a side of 1070 mm is considered. The side length of 1070 mm corresponds to 9 unit cells, with each

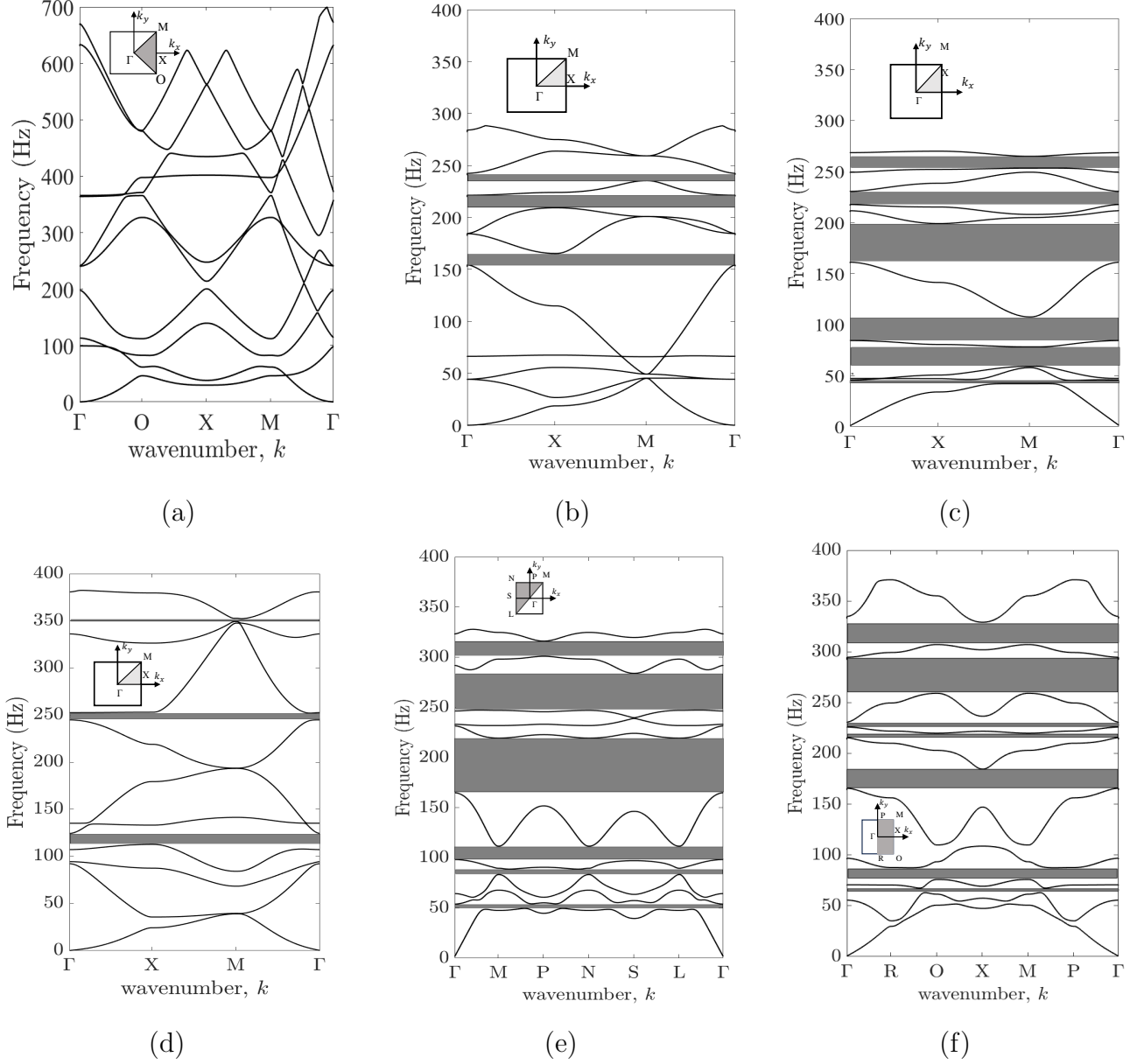
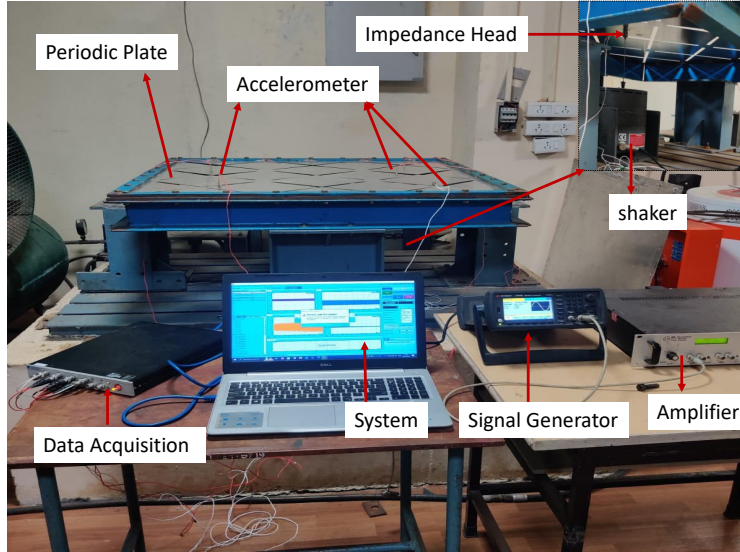


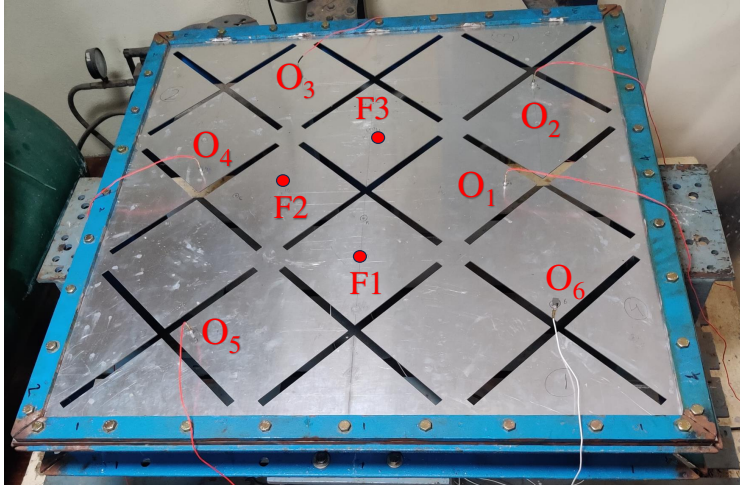
FIG. 5: Dispersion curves for the unit cell for a plate with various cutouts: (a) ellipse, (b) intersecting ellipses, (c) intersecting rectangular slots, (d) cross, (e) unequal intersecting slots with centre offset and (f) Intersecting slots with centre offset.

unit cell having an ‘x’ shape cutout(c.f. Figure 4c); the cutouts are manufactured using laser cutting. To demonstrate the effectiveness of this cutout on vibration isolation, the experiments and the FE simulations were carried out on a solid aluminum plate as well.

Figure 6a shows the experimental setup. The plate is clamped on all sides, and the shaker



(a)



(b)

FIG. 6: (a)Experiment Setup, (b) Plate with locations of input force and response measurement.

(MB Dynamics) is attached at the bottom of the plate. The signal generator (Keysight waveform generator) provides excitation to the shaker through an amplifier. The shaker tip has an impedance head (Dytran model 5860B) to measure the input force and acceleration, and accelerometers at multiple locations (Dytran model 3145AG) are used to measure the response. An 8-channel data acquisition system (Crystal Instruments) is used to acquire and process

sensor data.

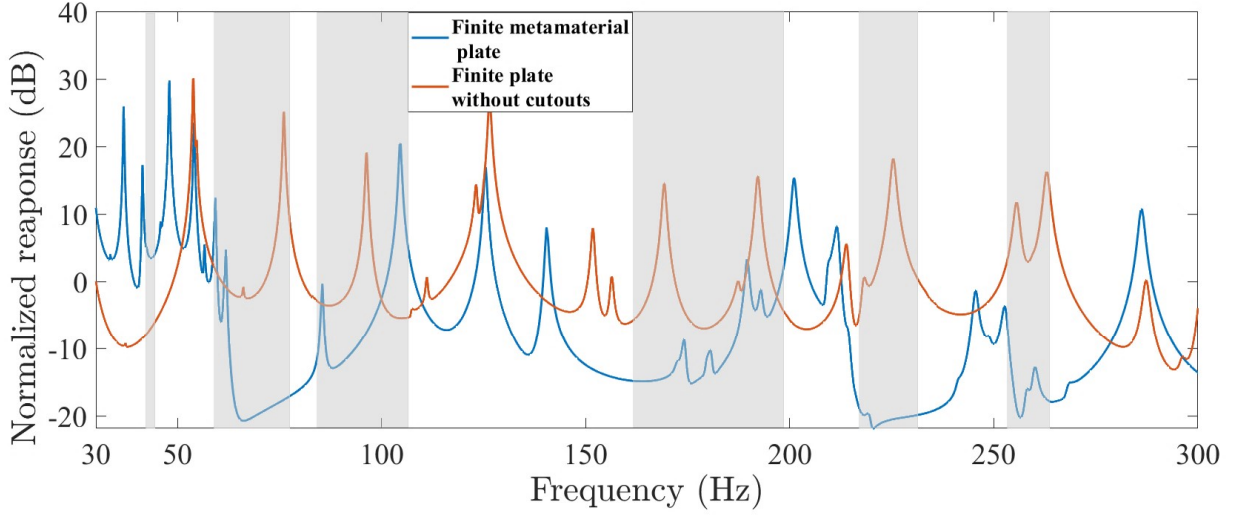
For the experiment, a sine sweep signal from 30 to 300 Hz is used for exciting the plate structure. The shaker is moved to three locations, F1, F2, and F3, as shown in Figure 6b; this is done to understand the effect of excitation location on the plate’s response. The shaker is placed at one of the three locations, and the response is measured at 6 locations (O_i , $i = 1, \dots, 6$), as shown in Figure 6b. Four averages are used at each accelerometer measurement location to reduce signal noise. A composite root mean square (RMS) acceleration is obtained from the accelerations measured at the various locations as $a_{RMS} = \sqrt{\frac{\sum_{i=1}^N a_i^2}{N}}$; in our case $N = 6$. This is normalized with the RMS value of the acceleration at the excitation location. We do this so that a single metric can be used to compare the effect of excitation location and the effect of cut-outs at different frequencies.

B. Results

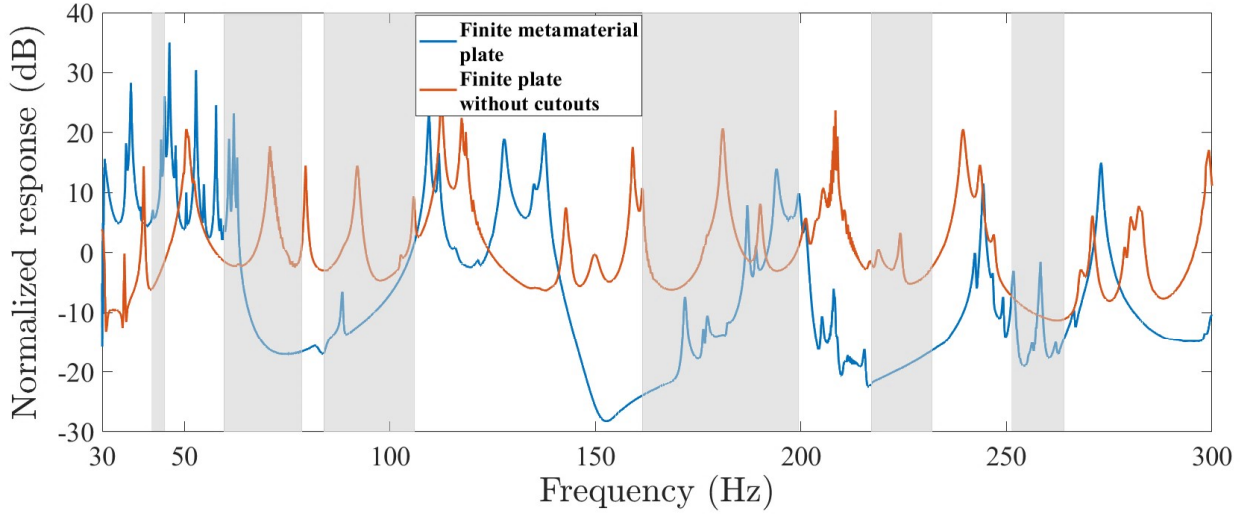
Next, the plates’ normalized response from FEM is compared with the experiment, using the same six measurement locations O_i , $i = 1, \dots, 6$ for different excitation locations, F_i , $i = 1, 2, 3$. A comparison between the periodic plate and the finite plate is also presented. In the forthcoming figures, the band gap obtained from the FE simulation on the periodic plate is highlighted with a ‘grey’ region.

For the excitation location F1, Figures 7a and 7b shows a comparison between the periodic plate and the solid plate normalized response obtained from FEM and experiment. The shaded regions represent the band gaps from the numerical study of the infinite periodic structure. It can be seen that the periodic plate response is lower than the solid plate for all the bands except in the first band gap region. The numerical simulations show that Bands 2 and 3 are smaller than the bandwidth in the unit cell model. The experimental results also show the same trend, but the 2nd and 4th frequency bands are smaller than the bandwidth the unit cell model predicted. The 5th and 6th band of the FEM and experiment response shows good agreement with the numerical band. Overall, one can see significant vibration reduction in the stop band regions both in FE simulations and experiments.

For the excitation location F2, Figures 8a and 8b shows a comparison between the periodic plate and the solid plate normalized response obtained from FEM and experiment. The shaded



(a)

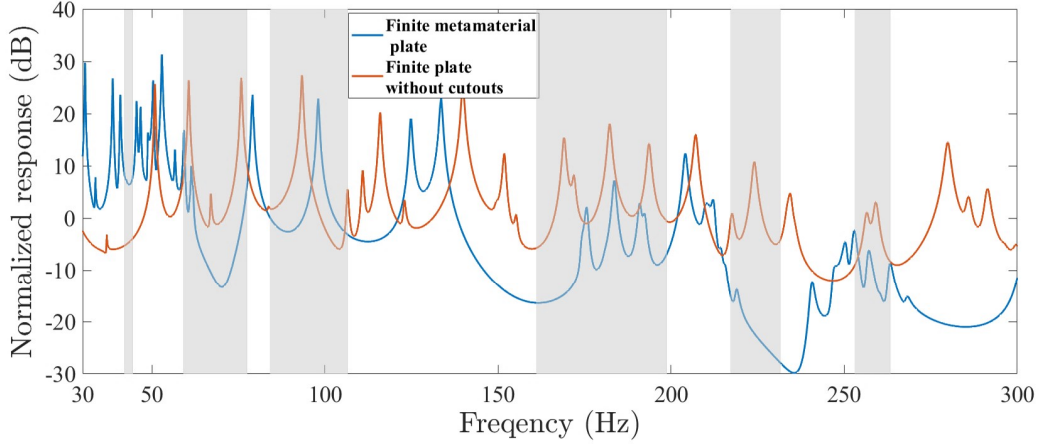


(b)

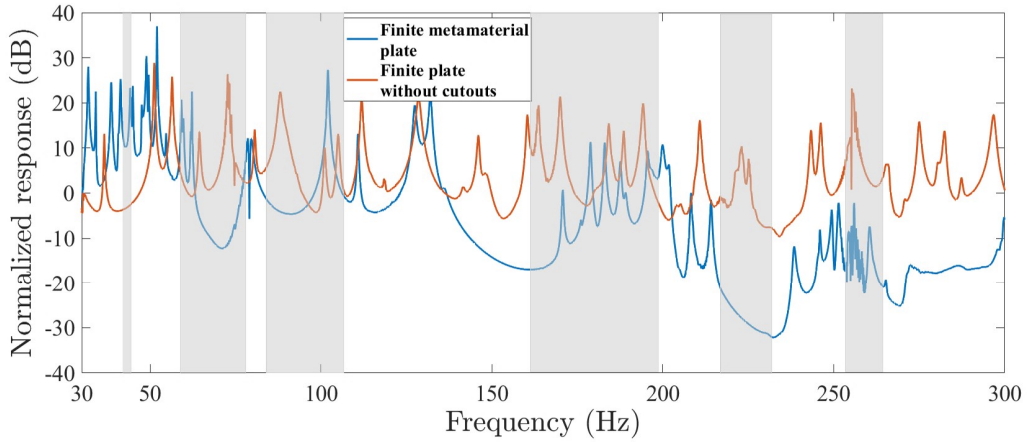
FIG. 7: Normalized Response for input at F1 (a)FEM (b) Experiment

regions again represent band gaps from the numerical study of the infinite structure. It can be seen that the FEM and experiment are consistent with each other. In the first band gap region, both FEM and experiment show higher response for the periodic plate when compared to the solid plate. In the 2nd band, the response of the periodic plate is lower than the solid plate, but the frequency band is smaller than the numerical band gap. For the third numerical band, the periodic plate shows not much improvement in both FEM and experiment. In the

experiment, the periodic plate response is lower but for a small frequency range in the 4th numerical band, while in FEM, the periodic plate response is lower in the complete band. Both FEM and experiment show good agreement with the numerical band (5th and 6th).



(a)

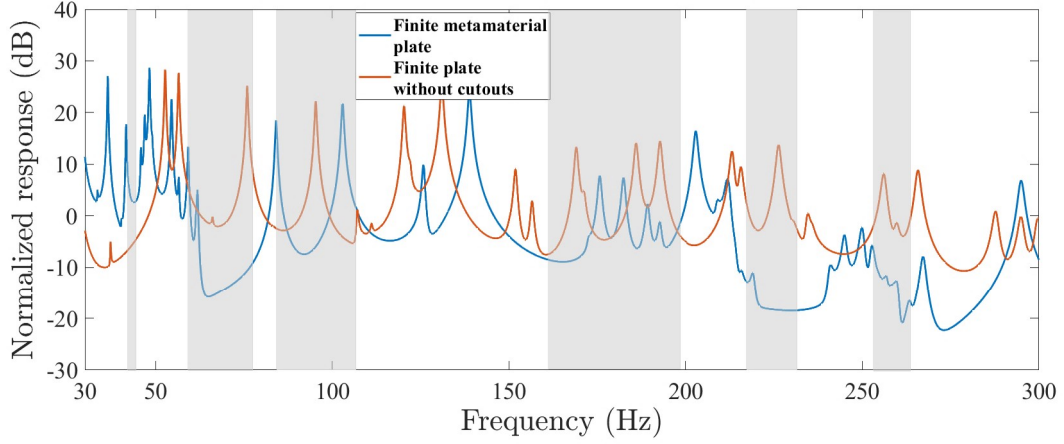


(b)

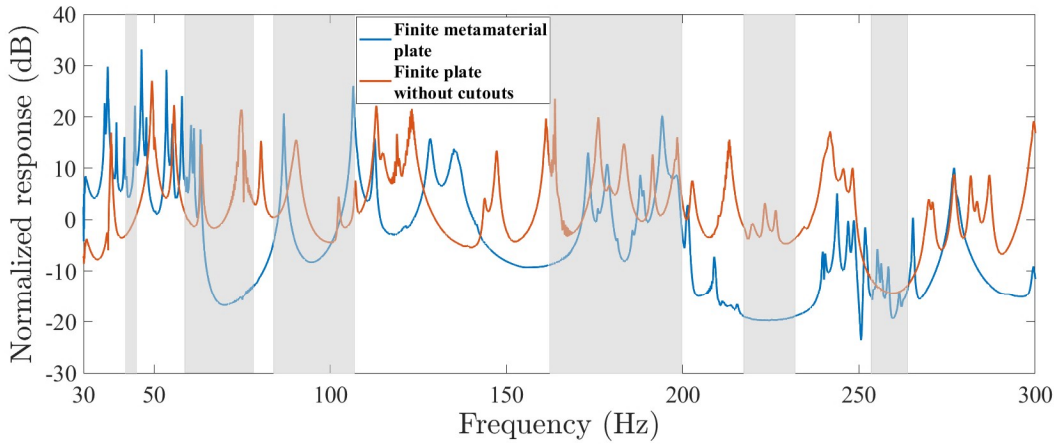
FIG. 8: Normalized Response for input at F2 (a)FEM (b) Experiment

For the excitation location F3, Figures 9a and 9b shows a comparison between the periodic plate and the solid plate normalized response obtained from FEM and experiment. In 1st band, both FEM and experiment show periodic plate response higher than solid plate. The frequency range for which periodic plate response is smaller than solid plate is smaller than the 2nd numerical band in both FEM and experiment. In the 3rd and 4th bands, the periodic plate does not show much of an improvement over the solid plate in both FEM and experiment. FEM

and experiment response shows good agreement with the numerical band. In the 6th band, the FEM shows good agreement with the numerical band, but in the experiment, the periodic plate show does not show much improvement.



(a)



(b)

FIG. 9: Normalized Response for input at F3 (a)FEM (b) Experiment

The first band gap periodic plate showed no attenuation in all three cases compared to the solid plate. It was also seen that the band gaps were smaller in the experiment. This is possibly due to the use of a 3×3 finite plate grid. It would be good to examine this using a larger grid (5×5), but the plate size is quite significant to perform experiments in the lab ($1.65\text{m} \times 1.65\text{m}$). Although, in theory, the plate should be square, the experimental plate after assembly exhibited a small deviation from the 1:1 aspect ratio. This, along with the nonuniformity of the clamping

at some places, leads to the generation of closely spaced frequencies for some modes. Even with these issues, the finite periodic plate does show significant vibration reduction in the predicted band gaps.

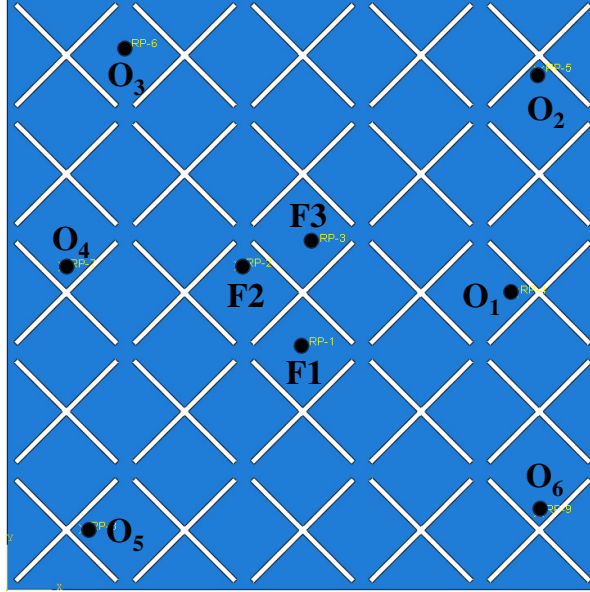


FIG. 10: Schematic representation of a 5×5 periodic plate. Note that F_i , $i = 1, 2, 3$ are the input location and O_j , $j = 1, \dots, 6$ are the locations where the response is measured.

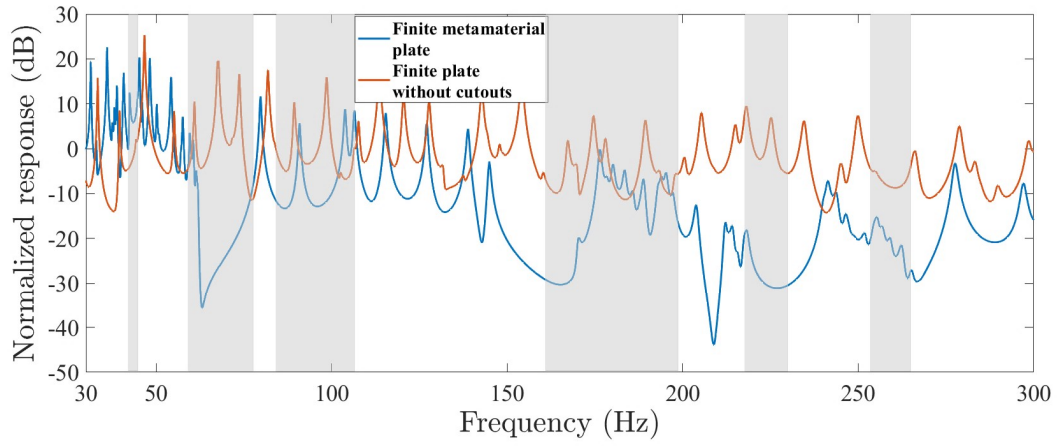
A 5×5 periodic plate is examined, similar to the 3×3 plate, using the FE model. Figure 10 shows a 5×5 periodic plate with input and output measuring locations. Figure 11a shows the normalized response for input at location F1. Figure 11a shows that the 2nd, 5th and 6th band periodic plates have responses lower than the solid plates. For the 3rd and 4th bands, the periodic plate has a lower response than the solid plate in the frequency range smaller than the band from unit cell studies. Figure 11b shows the response for input at F2. From Figure 11b, it can be seen that for the 2nd band, the periodic plate shows a slightly lower response than the solid plate. Periodic plate show little improvement over solid plate in 3rd band. For the 4th band, the periodic plate shows an overall lower response than the solid plate. In the 5th and 6th bands, periodic plates respond lower than solid plates. The Figure 11c shows the response for input at F3. In the second gap, the periodic plate has a lower response than the solid plate. In the 3rd band, the periodic plate shows no improvement over the solid plate; the same is in the 4th band. Periodic plate shows lower response than solid plate in the 5th and 6th bands.

The response of the 5×5 periodic plate shows the same trend as that of the 3×3 periodic plate. However, after 200 Hz, the 5×5 periodic plate shows a considerably reduced response than the 3×3 periodic plate. At lower frequencies, the effect of periodic plate size on the response does not differ much. The smaller size 3×3 periodic plate shows reasonable attenuation in the frequency range of interest, which makes it practically viable.

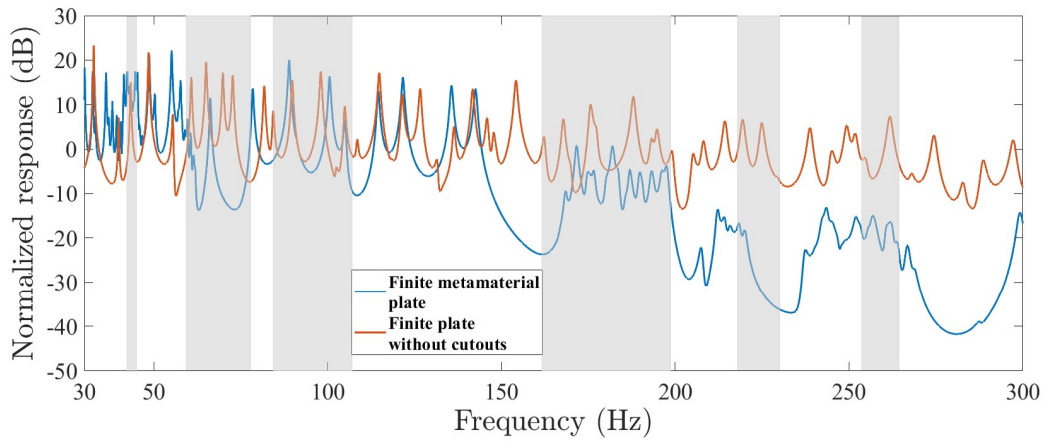
V. CONCLUSION

In this paper, the band gap properties of the unit cells with different geometrical shapes for low-frequency regions are studied. The finite element method (FEM) is used to obtain the band gaps. The effect of various geometrical holes on band gaps is discussed. A band gap properties in a finite periodic plate are examined experimentally. From the numerical and experimental study, the following conclusion can be drawn:

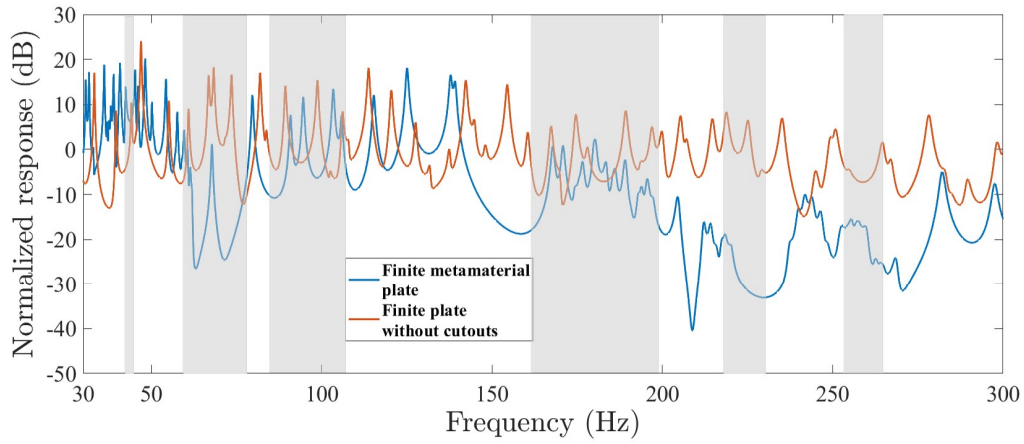
1. The band gap behavior for different geometries such as ellipse, two diagonal cross ellipses, two diagonal intersecting rectangular slots, intersecting rectangular slots, and offset diagonal rectangular slots have been examined for their band gap properties in the low-frequency region.
2. From the study, it is clear that a high aspect ratio X-type rectangular slots passing through the center are essential to create band gaps in the lower modes. In fact, for the first time, the paper demonstrates the presence of band gaps in the first and second as well as between the third and fourth modes. This has been done keeping the porosity level at around 10%, which is a significant finding.
3. A finite plate composed of a 3×3 unit cell arrangement was fabricated and tested for its response to sinusoidal excitation. A FE simulation was also carried out to compare the results obtained from the experiment. Three locations were chosen for the excitation, and the response was averaged over six spread-out locations on the plate. The results demonstrate that the proposed geometry can reduce vibration significantly in the band gap regions.



(a)



(b)



(c)

FIG. 11: 5×5 periodic plate normalized response (FEM) for input at (a) F1 (b) F2 (c) F3

DATA AVAILABILITY

The data supporting this study’s findings are available from the corresponding authors upon reasonable request.

REFERENCES

- ¹L Ai and X-L Gao. Metamaterials with negative poisson’s ratio and non-positive thermal expansion. *Composite Structures*, 162:70–84, 2017.
- ²Dingkang Chen, Huan Zi, Yinggang Li, and Xunyu Li. Low frequency ship vibration isolation using the band gap concept of sandwich plate-type elastic metastructures. *Ocean Engineering*, 235:109460, 2021.
- ³Wenjiong Chen, Xiangyu Tian, Renjing Gao, and Shutian Liu. A low porosity perforated mechanical metamaterial with negative Poisson’s ratio and band gaps. *Smart Materials and Structures*, 27(11):115010, 2018.
- ⁴Sachchidanand Das, Kush Dwivedi, Sabareesh Geetha Rajasekharan, and Yendluri V Das-eswara Rao. Vibration attenuation and bandgap characteristics in plates with periodic cavities. *Journal of Vibration and Control*, 27(7-8):827–838, 2021.
- ⁵Jie Deng, Ling Zheng, and Nansha Gao. Broad band gaps for flexural wave manipulation in plates with embedded periodic strip acoustic black holes. *International Journal of Solids and Structures*, 224:111043, 2021.
- ⁶Yuqiang Gao and Lifeng Wang. Ultrawide coupled bandgap in hybrid periodic system with multiple resonators. *Journal of Applied Physics*, 127(20), 2020.
- ⁷Jian-kun Huang, Xiong-wei Liu, Xin-hua Chen, and Hong-jun Xiang. Multiple flexural-wave attenuation zones of periodic slabs with cross-like holes on an arbitrary oblique lattice: Numerical and experimental investigation. *Journal of Sound and Vibration*, 437:135–149, 2018.
- ⁸Jiankun Huang, Zhifei Shi, and Weixin Huang. Multiple band gaps of phononic crystals with quasi-sierpinski carpet unit cells. *Physica B: Condensed Matter*, 516:48–54, 2017.
- ⁹Farhad Javid, Pai Wang, Ali Shaniyan, and Katia Bertoldi. Architected materials with ultra-low porosity for vibration control. *Advanced materials*, 28(28):5943–5948, 2016.

- ¹⁰Gaofeng Jia and Zhifei Shi. A new seismic isolation system and its feasibility study. *Earthquake Engineering and Engineering Vibration*, 9:75–82, 2010.
- ¹¹Yabin Jin, Shixuan Zeng, Zhihui Wen, Liangshu He, Yong Li, and Yan Li. Deep-subwavelength lightweight metastructures for low-frequency vibration isolation. *Materials & Design*, 215:110499, 2022.
- ¹²Bing Li, Chao Zhang, Fang Peng, Wenzhi Wang, Bryan D Vogt, and KT Tan. 4d printed shape memory metamaterial for vibration bandgap switching and active elastic-wave guiding. *Journal of Materials Chemistry C*, 9(4):1164–1173, 2021.
- ¹³Jinqiang Li, Yao Zhang, Xinlei Fan, and Fengmin Li. Multi bandgaps design of sandwich metamaterial plate with embedded membrane-type resonators. *Journal of Sandwich Structures & Materials*, 25:311–329, 2023.
- ¹⁴Suobin Li, Yihua Dou, Tianning Chen, Zhiguo Wan, Jingjing Huang, Bing Li, and Fan Zang. Evidence for complete low-frequency vibration band gaps in a thick elastic steel metamaterial plate. *Modern Physics Letters B*, 33(4):1950038, 2019.
- ¹⁵Yingli Li, Shiguang Yan, and Yong Peng. Broadband vibration attenuation characteristic of 2d phononic crystals with cross-like pores. *Thin-Walled Structures*, 183:110418, 2023.
- ¹⁶Xiaojian Liu, Youhua Fan, and Yumin An. The influence of t-square fractal shape holes on the band structure of two-dimensional phononic crystals. *Physica B: Condensed Matter*, 429:73–78, 2013.
- ¹⁷Fariha Mir, Debdyuti Mandal, and Sourav Banerjee. Metamaterials for acoustic noise filtering and energy harvesting. *Sensors*, 23(9):4227, 2023.
- ¹⁸Vinícius F. Dal Paggetto and Alberto L Serpa. Flexural wave band gaps in a ternary periodic metamaterial plate using the plane wave expansion method. *Journal of Sound and Vibration*, 495:115909, 2021.
- ¹⁹HYY Shi, TE Tay, and HP Lee. Elastic wave propagation in perforated plates with tetrad elliptical structural hierarchy: Numerical analysis and experimental verification. *Journal of Sound and Vibration*, 448:73–82, 2019.
- ²⁰BR Somashekar, G Prathap, and C Ramesh Babu. A field-consistent four-noded laminated anisotropic plate/shell element. *Computers & Structures*, 25:345–353, 1987.
- ²¹Xiaojun Tan, Bing Wang, Shuai Chen, Shaowei Zhu, and Yuguo Sun. A novel cylindrical negative stiffness structure for shock isolation. *Composite Structures*, 214:397–405, 2019.

- ²²Liling Tang and Li Cheng. Periodic plates with tunneled acoustic-black-holes for directional band gap generation. *Mechanical Systems and Signal Processing*, 133:106257, 2019.
- ²³Xiangyu Tian, Wenjiong Chen, Renjing Gao, Shutian Liu, and Jiaying Wang. Perforation-rotation based approach for band gap creation and enlargement in low porosity architected materials. *Composite Structures*, 245:112331, 2020.
- ²⁴Kai Wang, Ying Liu, and Tianshu Liang. Band structures in sierpinski triangle fractal porous phononic crystals. *Physica B: Condensed Matter*, 498:33–42, 2016.
- ²⁵Yan-Feng Wang, Yue-Sheng Wang, and Xiao-Xing Su. Large bandgaps of two-dimensional phononic crystals with cross-like holes. *Journal of Applied Physics*, 110(11), 2011.
- ²⁶W Xiao, GW Zeng, and YS Cheng. Flexural vibration band gaps in a thin plate containing a periodic array of hemmed discs. *Applied Acoustics*, 69:255–261, 2008.
- ²⁷Yong Xiao, Jihong Wen, and Xisen Wen. Flexural wave band gaps in locally resonant thin plates with periodically attached spring–mass resonators. *Journal of Physics D: Applied Physics*, 45(19):195401, 2012.
- ²⁸Y Xiong, Andi Xu, Shurui Wen, Fengming Li, and Seyed Mahmoud Hosseini. Optimziation of vibration band-gap characteristics of a periodic elastic metamaterial plate. *Mechanics of Advaned Materials and Structures*, 30:3204–3214, 2023.
- ²⁹Jian Xue, Weiwei Zhang, Jing Wu, Chao Wang, and Hongwei Ma. A semi-analytical method for vibration localization of plates integrated with low-frequency plate-type resonators. *Thin-Walled Structures*, 1994:1113332, 2024.
- ³⁰Gengwang Yan, Song Yao, and Yingli Li. Propagation of elastic waves in metamaterial plates with various lattices for low-frequency vibration attenuation. *Journal of Sound and Vibration*, 536:117140, 2022.
- ³¹Wencheng Yin, Jian Zhu, Zhiqiang Tong, Leilei Wang, Dichen Li, and Liang Wang. 3d printed three-dimensional elastic metamaterial with surface resonant units for low-frequency vibration isolation. *Virtual and Physical Prototyping*, 19:e2382159, 2024.
- ³²Yingjie Zhang, Wei Xu, Zhimin Chen, Junqiang Fu, and Lihang Yin. Design of tunable pneumatic metamaterials for low–frequency vibration control. *AIP Advances*, 14:062035, 2024.
- ³³Sahar Zouari, Julien Brocaïl, and J-M Génevaux. Flexural wave band gaps in metamaterial plates: A numerical and experimental study from infinite to finite models. *Journal of Sound*

and Vibration, 435:246–263, 2018.